J Mater Sci: Mater Electron (2021) 32:13068–13080

Structural, optical, magnetic, photocatalytic activity and related biological effects of $CoFe_2O_4$ ferrite nanoparticles

B. Yalcin[1], S. Ozcelik[2], K. Icin[3], K. Senturk[4], B. Ozcelik[5], and L. Arda[6,*]

[1] *Department of Medical Laboratory Techniques, Vocational School of Health Services, Bahcesehir University, 34353 Istanbul, Besiktas, Turkey*
[2] *Department of Food Engineering, Faculty of Engineering, Hakkari University, 30000 Hakkari, Turkey*
[3] *Department of Metallurgical and Materials Engineering, Faculty of Engineering, Karadeniz Technical University, Trabzon, Turkey*
[4] *Department of Mechatronics Engineering, Faculty of Engineering and Architecture, Istanbul Gelisim University, 34310 Istanbul, Turkey*
[5] *Department of Physics, Faculty of Science and Letters, Cukurova University, 01330 Adana, Turkey*
[6] *Department of Mechatronics Engineering, Faculty of Engineering and Natural Sciences, Bahcesehir University, 34353 Istanbul, Besiktas, Turkey*

Received: 16 January 2021
Accepted: 12 March 2021
Published online: 5 May 2021

ABSTRACT

The synthesis of magnetic nano-sized spinel ferrites has become an important area of research, due to their several potential applications. In this work, $CoFe_2O_4$ nanoparticles were synthesized by the co-precipitation method. Structural, magnetic, and photocatalytic properties of cobalt ferrites were analyzed based on their chemical composition considering their biological properties. Structural and morphological properties were investigated by X-ray diffraction analysis (XRD) and scanning electron microscope (SEM), respectively. Lattice parameters and cell volumes were calculated from XRD data. SEM images revealed uniform surface morphology and spherical shape of nanoparticles. Magnetization measurements were measured by using Lake Shore 7304 model Vibrating Sample Magnetometer (VSM). In hemolytic activity tests, formation of a precipitate with a characteristic black color provided an explicit evidence to the formation of heme–iron complexes. Undesirable hemolytic effect of $CoFe_2O_4$ nanoparticles on human erythrocytes at both concentrations was attributed to the comparatively high amount of reactive oxygen species formed by $CoFe_2O_4$ nanoparticles. The theoretical concentration C_o (theory) obtained by second-order model (0.82 mg/L) fit with the experimental value of C_o (experimental) (0.95 mg/L) well in photocatalytic activity tests.

Address correspondence to E-mail: lutfi.arda@eng.bau.edu.tr

https://doi.org/10.1007/s10854-021-05752-6

1 Introduction

In recent years, nano-sized metal oxide particles have been widely investigated due to their huge contact area between materials, good mechanical, and electrical properties arising from the adjustment of dimensions.

Especially, nano-sized iron oxides have gained extreme attention due to their unique material properties, such as high surface/volume ratio, excellent photostability, and high quantum yield [1]. They become very popular in the fields of optics, electronics, chemical sensors, bio-imaging applications, and medicine. The ability to control the behavior of the nanomaterials using an external magnetic field leads to potential applications, including magnetic resonance imaging, controlled drug delivery, and magnetic hyperthermia [2, 3]. Nanoparticles, which are planning to be used for such applications, should have a low-toxic nature, high stability, significant selectivity of accumulation in targeted area, and superparamagnetic properties at room temperature [4].

For instance, superparamagnetic particles were found positively responsive toward erythrocytes [5, 6] and some cancer cells, such as lung and breast cancer even without immunospecific coatings [7, 8]. $NiCo_2O_4$ [9, 10], $CuCo_2O_4$ [11], and $MnFe_2O_4$ [12, 13] nanoparticles were also investigated for their morphological, electrical, magnetic, and photocatalytic properties, which are directly related to their biomedical application performance. Besides iron oxide, binary iron oxides and other iron containing nanomaterials also have magnetic properties which are essential for biomedical applications. Especially, the spinel ferrites have gained considerable scientific and technological interest due to their unique physical and chemical properties as well as their technological applications.

Spinel ferrites can be represented by the formula of MFe_2O_4 with a face-centered cubic structure where *M* is a divalent cation, such as Co, Cu, Ni, Mn, or Fe, and commonly synthesized by sol–gel method [14]. Among spinel ferrites, copper ferrite ($CuFe_2O_4$) and cobalt ferrite ($CoFe_2O_4$) are of great interest from physics, chemistry, and biomedical aspects because of their excellent chemical and mechanical stability, high magnetocrystalline anisotropy, and high coercivity [15–17].

Improved mechanical hardness and stability of $CoFe_2O_4$ under physiological conditions and tunable superparamagnetic behavior by changing particle size [18] make these nanomaterials a tough competitor over other magnetic materials, such as traditional iron oxides, Fe_3O_4 and Fe_2O_3. Moreover, undesirable interactions of red blood cells (RBCs) and traditional iron oxides could be prevented by ferrites providing better hemocompatibility [19]. A scientific method to adjust the toxicity of nano-sized materials is to apply biocompatible coatings, such as polysiloxane, alginate, and citric acid, to the surface [20, 21]. A study by Laznev et al. revealed that there was no significant difference in the cytotoxicity of $CoFe_2O_4$ and polysiloxane surface-coated $CoFe_2O_4$ nanoparticles [22]. $CoFe_2O_4$ nanoparticles were also revealed as promising nanocarriers in controlled drug delivery applications [23]. Cai et al. studied the controlled release of doxorubicyn (an anticancer drug) from three–dimensional $CoFe_2O_4$ nanospheres synthesized by hydrothermal method. $CoFe_2O_4$ nanospheres were shown to have a high loading capacity of 88.6% and a promising drug release capacity of 55% under alternating magnetic field [24]. Manohar et al. [25, 26] investigated magnetic, dielectric, and photocatalytic properties of both manganese- and zinc-doped Fe_2O_4 nanoparticles. They claimed both nanomaterials synthesized by solvothermal method as promising in the field of biomedical applications.

It appears from our literature research that spinel ferrites were used in various areas, including catalysis and water treatment. Ferrites were also introduced as promising materials for especially biomedical applications. However, the interactions between these nano-sized materials and tissues and blood components are still an uncompleted issue. Thus, it is still an open question whether these nanomaterials are suitable to be used in vivo applications or cause any undesired interactions between the cells of living tissues. This research reports the synthesis and material properties of $CoFe_2O_4$ nanoparticles together with their blood compatibilities. In this study, we were also concerned about the photodegradation mechanism of crystal violet (CV) by $CoFe_2O_4$ nanoparticles which has not been studied sufficiently. This study aims to investigate and clarify basic biological effects of these nanoparticles for their potential use in biomedical area. Concurrently, we aimed to assess whether $CoFe_2O_4$ nanoparticles could

be used as an effective photocatalyst in water treatment.

2 Experimental procedures

2.1 Nanoparticle synthesis

In this study, all spinel ferrites were prepared by the co-precipitation methods. Iron(III) nitrate nonahydrate ($FeN_3O_9{\cdot}9H_2O$) and Cobalt(II) nitrate hexahydrate ($Co(NO_3)_2{\cdot}6H_2O$) were used to fabricate nanocrystalline Co-spinel ferrites. All nitrates used in co-precipitation method are of analytical graded Alfa Aesar. The weights used in experimental runs ($FeN_3O_9{\cdot}9H_2O$; $Co(NO_3)_2{\cdot}6H_2O$) were determined according to stoichiometry between both ferrites and nitrates. The solution mixture of 0.2 M $FeN_3O_9{\cdot}9H_2O$ and 0.1 M $Co(NO_3)_2{\cdot}6H_2O$ were dissolved in 100 mL of deionize water. A few drops of oleic acid (approximately 30 µL) were added to the mixture as surfactant. The solutions were mixed in a continuous mode for 2 h by Bandelin Sonopuls model ultrasonic homogenizer at 80 °C in water bath for homogeneous temperature distribution. After 2 h of stirring, NaOH was added drop by drop to obtain pH 9 under ultrasonic homogenizer for 1 h. At the end of process, precipitate was obtained. The precipitates were centrifuged five times using distilled water at 5000 rpm for 10 min by the NUVE NF400 model. The washed precipitates were dried at 80 °C under vacuum atmosphere for 8 h. Calcination process for $CoFe_2O_4$ nano-sized particles was carried out at 500 °C in air condition for 2 h.

2.2 Structural analysis

The structure of the $CoFe_2O_4$ nanoparticles was characterized by XRD measurements using a PANalytical X'pert Powder^3 model X-ray diffractometer device with CuKα ($\lambda = 1.5418$) radiation at room temperature in the scan range of $2\theta = 10°–90°$ with a scan speed of 3°/min and a step increment of 0.02°. The surface morphologies of precipitated powders were examined by using a SEM of the Zeiss EVO MA model. Optical properties of the CoFe2O4 nanoparticles were measured by using Shimadzu 2600 UV-Spectrometer with an integrating sphere in 300–1000 nm wavelength range. Magnetic hysteresis experiments were carried out in a Lake Shore model 7304 Vibrating Sample Magnetometer (VSM), operating within the 15–300 K temperature range.

2.3 Photocatalytic activity measurements

The photocatalytic activity of $CoFe_2O_4$ nanoparticles was investigated by photodegradation of CV under 254 nm irradiation. The concentration values of nanoparticle dispersion and CV solution were 1.0 mg/mL and 2.5×10^{-6} M, respectively. Distilled deionized water (DDW) obtained from Human Zeneer Power1 water purification system was used in the experiments. CV solutions containing the appropriate amount of nanoparticles were kept under magnetic stirring for 30 min (in darkness) to establish an adsorption/desorption equilibrium of CV molecules on the nanoparticle surface. After 30 min, 254 nm irradiation of CV-nanoparticle suspensions was started under continuous magnetic stirring. Aliquot parts were taken at appropriate time intervals and centrifuged at 4000 rpm to precipitate suspended nanoparticles. The absorption maxima of each supernatant was verified using a UV/Vis spectrophotometer (Shimadzu UV mini 1240) at a wavelength of 591 nm corresponding to the absorption maxima of CV. Distilled water was used as reference.

Photocatalytic properties of spinel ferrite nanoparticles were investigated using three different kinetic models, namely, zero order, first order and second order given by Eqs. 1, 2, and 3 [27–29].

Zero order:

$$C = C_o - kt \tag{1}$$

First order:

$$\ln\left(\frac{C_o}{C}\right) = k_1 t \tag{2}$$

Second order:

$$\frac{1}{C} = \frac{1}{C_o} + k_2 t, \tag{3}$$

where C_o and C represent the initial concentration of CV at $t = 0$ and the concentration of CV after a certain irradiation time (t), respectively. k, k_1, and k_2 were the rate constants for photocatalytic degradation.

2.4 Blood compatibility tests

Hemolytic activity of $CoFe_2O_4$ ferrites against human erythrocyte membrane was investigated. 0.108 mM

aqueous solution of trisodium citrate was used as stabilizing agent to prevent the coagulation of whole blood samples collected from healthy volunteers. Blood:anticoagulant ratio was adjusted as 9:1. Phosphate buffer solution (PBS) having a pH of 7.35 was prepared using $Na_2HPO_4{\cdot}2H_2O$ (1.78 g/L), KH_2PO_4 (0.24 g/L), KCl (0.2 g/L), and NaCl (8 g/L), then autoclave sterilized at 1 atm and 121 °C for 15 min. Ca- and Mg-free PBS was used to dilute the anticoagulated whole blood samples. RBCs were separated from plasma by centrifugation at 4000 rpm for 5 min. Precipitated RBCs were diluted up to 50 mL by adding PBS. 1.0 mg/mL and 5.0 mg/mL concentrations of $CoFe_2O_4$ suspensions were prepared and mixed with 0.8 mL of RBC stock solution. DDW and PBS were used in positive and negative control tests, respectively. In positive control test DDW causes complete (100%) hemolysis of all erythrocytes and negative control test corresponds to 0% hemolysis.

RBCs were incubated in the presence of varying nanoparticle concentrations under magnetic stirring at 37 °C for 3 h. Each test was performed twice. At the end of the incubation period, the samples were centrifuged at 3000 rpm for 5 min and the absorbance (ABS) value of supernatant was used to quantify the degree of hemoglobin release into the medium following cell lysis. Percent hemolysis values were calculated using the ABS value at 540 nm using the equation given below [30]:

$$\%\,\text{Hemolysis} = \frac{\text{ABS}_{\text{test sample}} - \text{ABS}_{\text{negative control}}}{\text{ABS}_{\text{positive sample}} - \text{ABS}_{\text{negative control}}}. \quad (4)$$

3 Results and discussions

3.1 XRD analysis

The X-ray diffraction (XRD) was used to investigate the crystalline phases of $CoFe_2O_4$ nanoparticles. The XRD of the $CoFe_2O_4$ ferrite nanoparticles is shown in Fig. 1.

As shown in Fig. 1, it can be observed that $CoFe_2O_4$ nanoparticles are spinel cubic structure of space group Fd-3m without secondary phases, which corresponds to PDF Card No.: 98-019-1044. The lattice parameter, a, was calculated from the diffraction pattern by using Eq. 5:

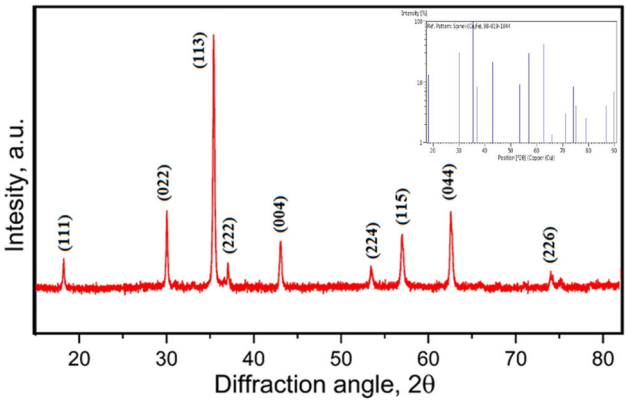

Fig. 1 X-ray diffraction patterns of $CoFe_2O_4$ ferrite nanoparticles. The inset shows the PDF card of $CoFe_2O_4$ NPs

$$a = d_{hkl}\left(h^2 + k^2 + l^2\right)^{1/2}. \quad (5)$$

The crystallite size of the $CoFe_2O_4$ nanoparticles was calculated from the full width at half maximum (FWHM) of the most intense peak (113) using the Debye–Scherrer equation:

$$D = 0.9\lambda/\beta\cos\theta_B, \quad (6)$$

where λ is the X-ray wavelength of CuKα, β is the FWHM of the diffraction peaks, and θ_B is the angle of Bragg diffraction. The calculated crystallite size (D) and lattice parameter (a) of $CoFe_2O_4$ nanoparticles for (113) peak were 39.2601 nm and 8.40 Å, respectively.

3.2 SEM analysis

The morphology of $CoFe_2O_4$ nanoparticles was studied using Scanning Electron Microscope (SEM) as shown in Fig. 2. As can be observed from Fig. 2a–d, the particles do not have a complete shape because they are agglomerated. As the resolution decreases, the structure appears dense and molten (Fig. 2a, b). On the other hand, as the resolution increases, the structure looks like snowflakes (Fig. 2d). The basic composition of all $CoFe_2O_4$ nanoparticles was provided by the EDS analysis illustrated in Fig. 3. All peaks in EDS analysis belong to $CoFe_2O_4$ nanoparticles. There are no other undesirable extra elemental peak additives.

3.3 Band gap calculation

The reflectance spectra of the $CoFe_2O_4$ nanoparticles, obtained by UV–Vis diffuse reflectance

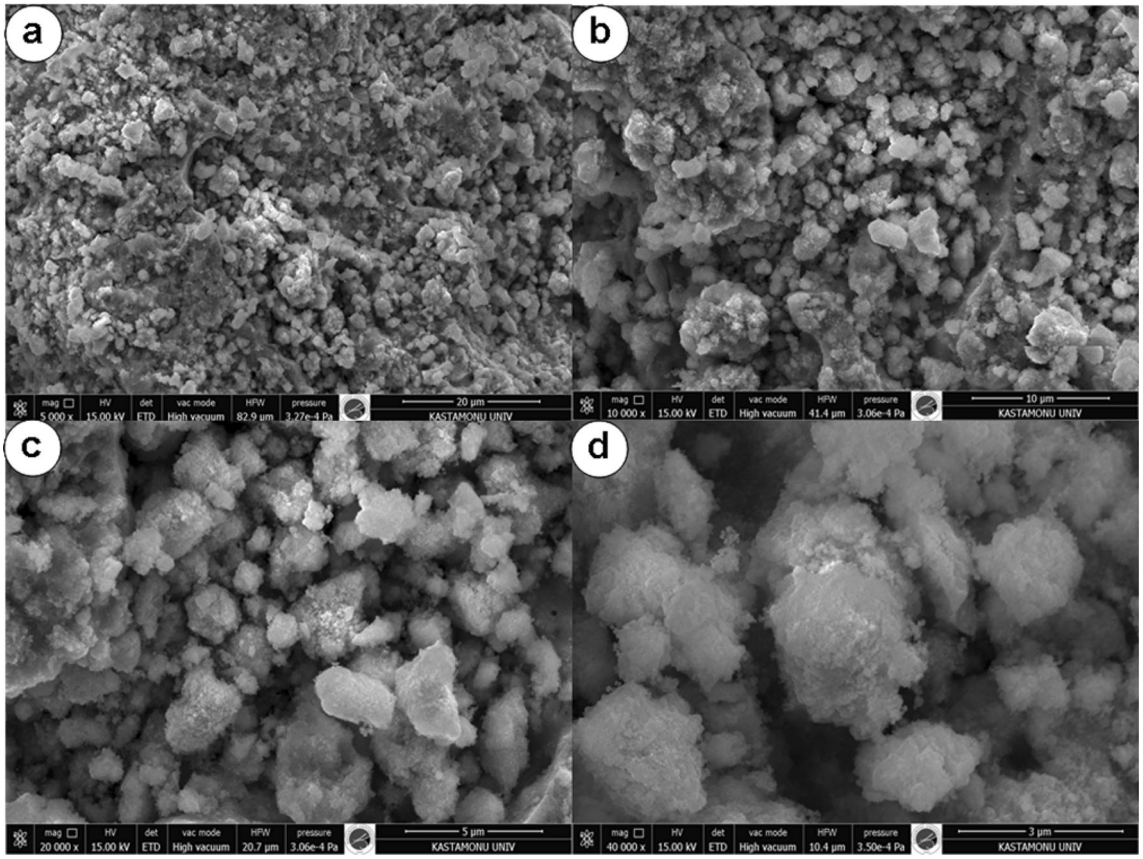

Fig. 2 SEM images of $CoFe_2O_4$ nanoparticles for 20, 10, 5, and 3 µm magnifications in **a**, **b**, **c**, and **d**, respectively

Fig. 3 EDS graph of $CoFe_2O_4$ nanoparticles

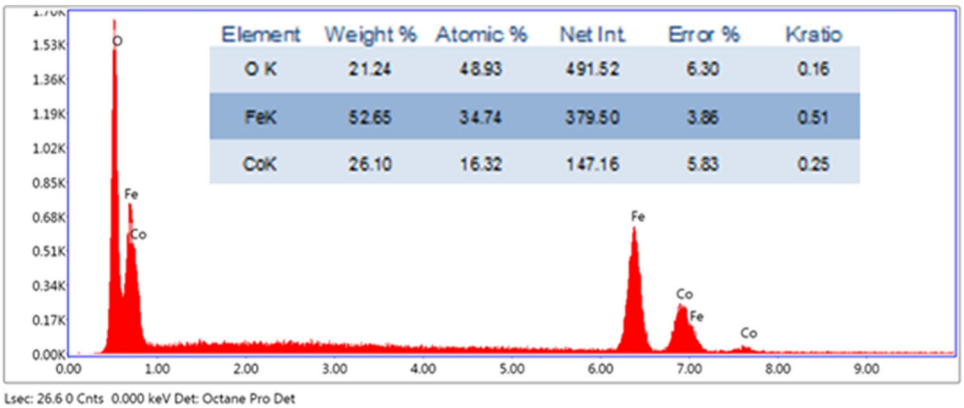

measurements (DRS) within the range of 0–700 nm wavelength. Notice that the graph inset in Fig. 4 has an absorption edge close to 140 nm. The Kubelka–Munk function was used to calculate the reflection ratio $F(R)$, which is proportional to the absorption coefficient (α) [30]:

$$F(R) = \frac{(1-R)^2}{2R}. \tag{7}$$

The following equation can be used to determine the optical band gap E_g for the photon energy ($h\nu$) and the absorption coefficient (α):

$$\alpha h\upsilon = k\left(h\upsilon - E_g\right)^{1/n}. \tag{8}$$

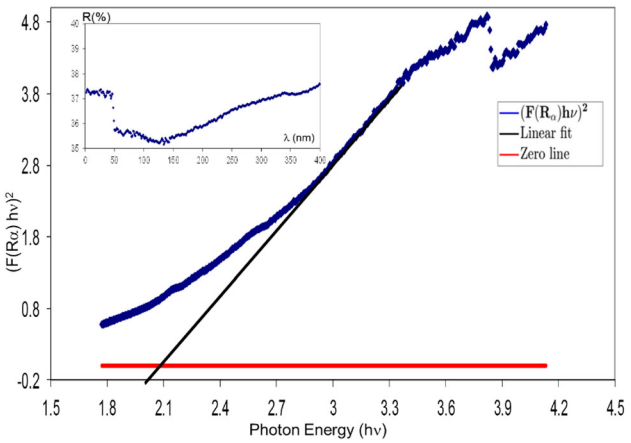

Fig. 4 The plots of $(F(R_\alpha)h\upsilon)^2$ as a function of photon energy ($h\nu$) and the linear fit for the $CoFe_2O_4$ nanoparticles

In Eq. (8), E_g and k are the optical band gap and energy-independent constants, respectively. $F(R_\alpha)$ is proportional to α and n is a constant that depends on the band gap type 1/2 and 2 for direct and indirect band gaps, respectively. Thus, for directly allowed transitions, n is taken as 2. Equation (8) can be transformed to

$$F(R_\alpha)h\upsilon = k\left(h\upsilon - E_g\right)^2. \tag{9}$$

In other words, $(F(R_\alpha)h\upsilon)^2 = k^2\left(h\upsilon - E_g\right)$. The slope of the graphs of $(F(R_\alpha)h\upsilon)^2$ was approximated by using a linear fit $y(h\upsilon) = A \times h\upsilon + B$ in the least-squares sense. To accomplish this, the error formula given in Eq. (10) was minimized for A and B:

$$E(A,B) = \min_{A,B} \sum_{i=1}^{N} \left[A \times (h\upsilon)_i + B - \left((F(R_\alpha)h\upsilon)^2\right)_i\right]^2, \tag{10}$$

where N is the number of data points. Table 1 displays A, B band gap energies E_g, and relative error value.

The direct and indirect band gap energies E_g, as shown in Table 1 and Fig. 4, were calculated by the linear approximation of the slope of the graph of $(F(R_\alpha)\ h\upsilon)^2$ to the photon energy axis where $F(R_\alpha) = 0$, namely, $E_g = h\upsilon = -B/A$, as plotted in Fig. 4. In other words, the intersection between the linear fit and the photon energy axis gave the value to E_g. The direct gap energies of the Coi-ferrite nanoparticles samples were observed as 2.1 eV as shown in Fig. 4 which was accurate within three decimal digits. The values of E_g depended on several factors, including lattice strain, carrier concentration, crystallite size, and the size effect of the dopant metals in Co-ferrite lattice.

Table 1 Calculating direct and indirect band gap energies for nickel ferrite with fitting curve function $y(h\upsilon) = A \times h\upsilon + B$

Sample	A	B	E_g	Relative error
$CoFe_2O_4$	3.14	−6.6	2.10	9.51×10^{-4}

3.4 Magnetic behavior

The interest in spinel ferrite $CoFe_2O_4$ NPs is due to their key properties, such as mechanical hardness, chemical stability, visible light absorption capacity, low band gap energy, and high saturation magnetization (M_s) values.

Vibrating Sample magnetometer (VSM) was used to characterize the magnetic nature of the $CoFe_2O_4$ nanoparticles. All measurements were taken in the range of ± 1 T at room temperature. The field dependence of magnetization is shown in Fig. 5. Moreover, the magnetic properties of spinel ferrites, such as M_s, remnant magnetization (M_r) and coercivity (H_c), are shown in Fig. 5. As shown in Fig. 5, the magnetization curve exhibits a narrow hysteresis. The M_s and coercivity field (H_c) values are depicted in Fig. 5, for the nanoparticles. Using the formula

$$M = M_s\left[1 - \frac{\beta}{H^2}\right], \tag{11}$$

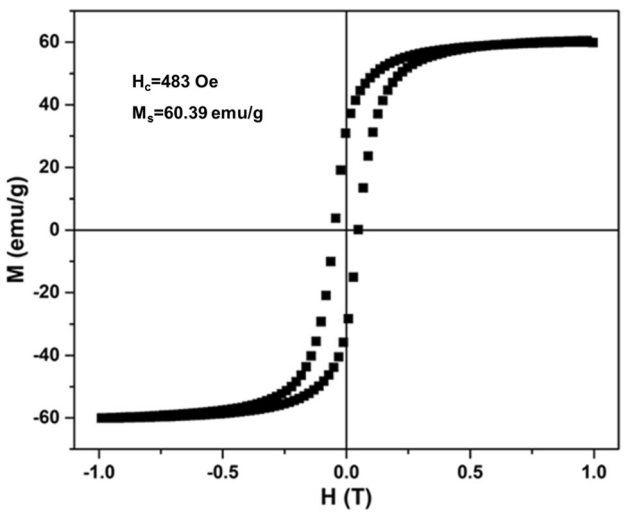

Fig. 5 M–H curves measured at $T = 300$ K for $CoFe_2O_4$ nanoparticles

the field dependence of the magnetization (M) close to the saturation value is calculated [31], where M_s is the saturation magnetization, β is a parameter related with the magnetocrystalline anisotropy, and H is the applied magnetic field.

The magnetization versus $1/H^2$ plots is shown in Fig. 6. β and M_s values of the $CoFe_2O_4$ nanoparticles determined from the slope of the linear fitting and the interception with the y-axis, respectively. The obtained values are depicted in Figs. 5 and 6. Once the β value is determined, the magnetic anisotropy constant (K_a) may be conveniently determined using Eq. 12 [31]:

$$K_a = M_s\sqrt{\frac{15\beta}{4}}. \quad (12)$$

The derived K_a value at 300 K is 2.26×10^5 erg/g.

The M_s value of $CoFe_2O_4$ nanoparticles obtained within the framework of this study is 60.39 emu/g, which is compatible with the studies in the literature [32]. Therefore, one can suggest that our $CoFe_2O_4$ NPs may be used in both biomedical and industrial fields.

3.5 Blood compatibility tests

The synthesis of magnetic nano-sized spinel ferrites has become an important area of research, due to their several potential applications [33–35]. Materials planned to be used in medical area must be well tested in terms of their biocompatibility. A hemolytic activity test is a suitable and scientific way of determination of biocompatibility of a synthetic material with living systems [36].

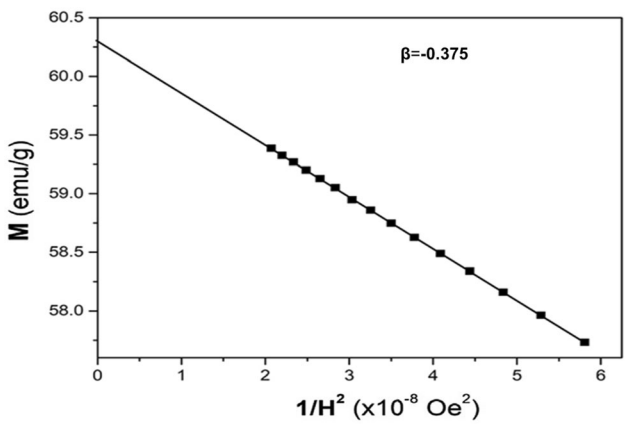

Fig. 6 Plots of M vs. $1/H^2$ obtained on representative samples at T = 300 K

In a related literature study, $CoFe_2O_4$ nanoparticles (30–50 nm) synthesized by the conventional microemulsion technique did not recommended to be used in intravenous drug administrations due to the negative findings of complete blood count [19]. However, some studies remark the impressive physicochemical properties of $CoFe_2O_4$ nanoparticles, like mechanical hardness, improved stability, and colloidal dispersibility under physiological conditions. Incompatibility between hemoglobin and iron containing materials arises from the presence of iron in the structure. These undesirable interactions could be prevented using ferrites for better tissue perfusion and hemocompatibility [37].

Nano-sized materials may change the morphology of RBCs or erythrocytes and cause hemolysis. Hemolysis is defined as the breakdown of cell membrane and lysis of cells. These undesirable interactions between nanoparticles and the blood may promote inflammatory and autoimmune disorders or leading infections as well as cancer by inducing the immune system to suppress [38]. In our study, $CoFe_2O_4$ were investigated in terms of their blood compatibility. Human erythrocytes drawn from healthy volunteers were used to investigate the hemolytic potentials of $CoFe_2O_4$ nanoparticles.

Figure 7 shows the UV–Vis spectra of erythrocyte suspensions treated with PBS alone (control) and $CoFe_2O_4$ nanoparticles with two different concentrations, which are 1.0 and 5.0 mg/mL. Hemolysis ratios corresponding to 1.0 mg/mL and 5.0 mg/mL

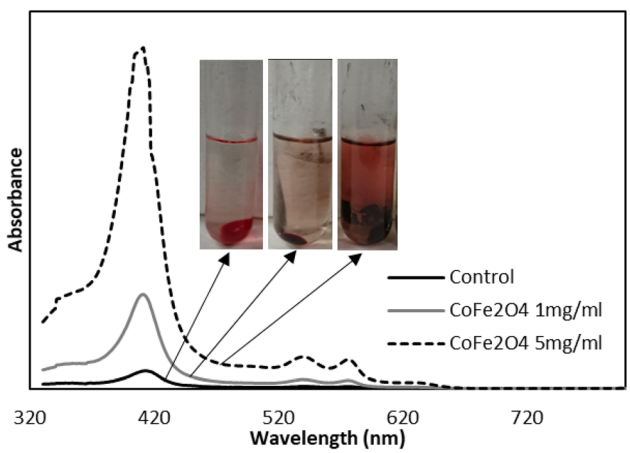

Fig. 7 UV–Vis spectra of erythrocyte suspensions treated with PBS alone (control) and $CoFe_2O_4$ nanoparticles with two different concentrations. The inset shows blood supernatant after centrifugation

concentrations were 5.4% and 24.7%, respectively. Hemolysis percentages lower than 5% are regarded as safe by International Standards Organization [39]. Thus, for both lower and higher concentrations of $CoFe_2O_4$, nanoparticles showed an undesirable hemolytic effect on human erythrocytes. This may be attributed to the comparatively high amount of reactive oxygen species formed by $CoFe_2O_4$ nanoparticles shown in photocatalytic activity tests (Fig. 8). Besides, a sharp increase for the absorption band at 408 nm corresponds to the strong oxidation of oxyhemoglobin to methemoglobin. Moreover, in $CoFe_2O_4$ test tubes, the precipitate with a characteristic black color provided an explicit evidence to indicate the formation of heme–iron complexes [40] (Fig. 7—inset photos).

Despite the fact that cobalt is a microelement essential for living organisms as it is the cofactor of cobalamin (vitamin B12), cobalt can have toxic effects at high concentrations. Cobalt compounds are classified as class II, which means they are not extremely toxic. However, cobalt compounds cause defects in protein and carbohydrate metabolisms, anemia, and carcinogenic and mutagenic effects [41]. Cobalt is a potential inducer of oxidative stress causing reactive oxygen species generation [42]. Reactive oxygen species (ROS) cause the oxidation of hemoglobin to methemoglobin (MHb). Methemoglobin forms when the ferrous (Fe^{2+}) ions in heme are oxidized to the ferric (Fe^{3+}) state, and the molecule will be unable to carry oxygen to tissues. MHb can form either spontaneously or be induced to form by many substances, including chlorites, phenolic compounds, and heavy metals, such as copper, zinc, and cobalt [43–45]. Normally, methemoglobin is reconverted to hemoglobin spontaneously by an enzymatic reduction within the cells. Cobalt may affect this mechanism by blocking the enzymatic activity [46]. Concisely, cobalt induced oxidation of heme and increasing concentration of methemoglobin was observed with increasing $CoFe_2O_4$ concentration. In conclusion, $CoFe_2O_4$ nanoparticles showed undesirable hemolytic effect in both 1 mg/mL and 5 mg/mL concentrations.

3.6 Photocatalytic activity measurements

Oxidative stress mediates several pathological changes, including not only the hemolysis but also the oxidation of sulfhydryl groups on the globin moiety of hemoglobin leading to oxidative denaturation, altered endothelial cell function leading vascular disorders, such as hypertension, stroke, and heart infarction. [47, 48]. Reactive oxygen species that are responsible for these undesirable pathologies can also be used to degrade organic pollutants, such as phenols, aromatic hydrocarbons, dyes, or pharmaceuticals in contaminated sources. Many nano-sized materials, which are used in medical applications and have magnetic properties, also have high electrical properties, low band gap values, and high surface area and also show catalytic effects. Combining high photocatalytic properties and biocompatibility is much more important in in vitro studies [49, 50].

Changes in the UV–Vis spectra of non-photodegraded CV in the presence of $CoFe_2O_4$ nanoparticles with the variation of time and second-order kinetic plot for photocatalytic degradation of CV over $CoFe_2O_4$ nanoparticles are shown in Fig. 8a, b. Decreasing absorption maxima at 591 nm indicated the degradation of CV by $CoFe_2O_4$ nanoparticles. Intensity of this characteristic band was gradually weakened in the first 420 min under the effect of 254 nm light and indicated the photodegradation of CV by $CoFe_2O_4$ nanoparticles.

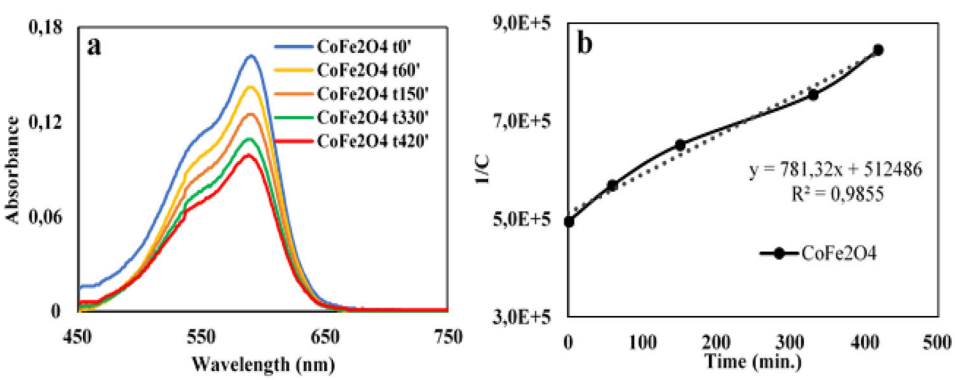

Fig. 8 UV–Vis spectra of CV as a function of time in the presence of **a** $CoFe_2O_4$ under 254 nm irradiation and **b** second-order kinetic plot for photocatalytic degradation of CV over $CoFe_2O_4$ nanoparticles

In this study, when ferrite nanoparticles were subjected to the 254 nm irradiation, Co^{2+} sites were excited with photo-generated electrons and Co^{3+} ions were produced (Eq. 13). This phenomenon could be a triggering case for the oxidation of iron in hemoglobin where ferrous form turns into ferric form and induces methemoglobin generation (Eq. 14).

Electron–hole pairs generated by radiation on the valence and conduction bands of semiconductors lead to the formation 19of ROS which are assumed to be responsible for the decomposition of organic molecules [51]. Photocatalytic decomposition mechanism of organic molecules under the effect of electromagnetic radiation has been well defined as an oxidative process in which three major steps were involved. In the fist step of photocatalytic degradation, electrons in valence band were excited by the radiation having energy higher than the band gap of semiconductor. Migration of the excited electrons to an empty conduction band leaves equal number of electron holes (h^{+}_{VB}) in the valence band. Second step is the migration of excited electrons to the surface.

Finally, the photo-generated electron–hole pairs take part in redox reactions, resulting in the formation of ROS. In this last step, photo-generated electrons are trapped by the oxygen and electron holes in the valence band interact with H_2O, resulting in the formation of superoxide ($O_2^{-\cdot}$) and hydroxyl radicals ($OH^{\cdot}$), respectively (Eqs. 15a and 15b). This step is followed by the formation of other reactive intermediates, including H_2O_2 and hydroperoxyl radical ($HOO^{\cdot}$) (Eq. 15c) [52]. Afterward, photo-generated electrons could be trapped by O_2 to form superoxide radicals ($O_2^{-\cdot}$), followed by the generation of other radical species ($O_2^{-\cdot}$, $HO^{\cdot}$, $HO_2^{\cdot}$). Also, the Co^{3+} sites can react with OH^{-} and return back into Co^{2+} to complete the photocatalytic circle (Eq. 17) [53]. Finally, the reactive species, including $O_2^{-\cdot}$, $HO^{\cdot}$, and $HO_2^{\cdot}$, possess sufficient energy for the photocatalytic degradation of CV (Eq. 18):

$$Co^{2+} + h\upsilon \rightarrow Co^{3+} + e^{-}, \tag{13}$$

$$Co^{3+} + Fe^{2+}(\text{ferrous}) \rightarrow Co^{2+} + Fe^{3+}(\text{ferric}), \tag{14}$$

$$e^{-} + O_2 \rightarrow O_2^{-\cdot}, \tag{15a}$$

$$h^{+}_{VB} + H_2O \rightarrow H^{+} + HO^{\cdot}, \tag{15b}$$

$$O_2^{-\cdot} + H^{+} \rightarrow HO_2^{\cdot} \rightarrow\rightarrow H_2O_2 + O_2, \tag{15c}$$

$$H_2O_2 + O_2^{-\cdot} \rightarrow HO^{\cdot} + HO^{-} + O_2, \tag{16}$$

$$Co^{3+} + HO^{-} \rightarrow Co^{2+} + HO^{\cdot}, \tag{17}$$

$$O_2^{-\cdot}, HO^{\cdot}, HO_2^{\cdot} + CV \rightarrow \text{Degradation products of CV}. \tag{18}$$

Kinetic parameters of zero-order, first-order and second-order rate equations for CV degradation in the presence of $CoFe_2O_4$ nanoparticles are listed in Table 2. Fitting the data of photocatalytic activity test to $(C) - t$ and to $\ln(C_o/C) - t$ showed that neither first-order nor second-order kinetic models were successful in representing the photodegradation kinetics of CV.

Second-order kinetic model was the best relationship that fits the degradation of CV by $CoFe_2O_4$ nanoparticles. Additionally, the theoretical concentration C_o (theory) obtained by second-order model (0.82 mg/L) fit with the experimental value of C_o (experimental) (0.95 mg/L) well. Briefly, it can be stated that the second-order kinetic model was the most acceptable model to describe the experimental kinetic data of CV photodegradation.

Photocatalytic properties of $CoFe_2O_4$ nanoparticles show significant CV degradation in 420 min under 254 nm irradiation and can be suitable to be used in wastewater treatment industries expurgating organic dyes. Moreover, $CoFe_2O_4$ nanoparticles were also responsible for concentration-dependent hemolysis ratios as shown by hemolysis assay (Fig. 7). Results were consistent because formation of ROS is considered as one of the main reasons of oxidative stress, resulting in lysis of erythrocytes.

Table 2 Kinetic parameters of three different kinetic models

Kinetic model	Parameters	Value
Zero-order	k	$8.2E^{-4}$ mg/L min
	R^2	0.9143
First-order	k_1	0.0012 L/min
	R^2	0.9458
Second-order	k_2	$1.91E^{-3}$ L/mg min
	C_o (experimental)	0.95 mg/L
	C_o (theory)	0.82 mg/L
	R^2	0.9855

4 Conclusion

$CoFe_2O_4$ nanoparticles were prepared by the co-precipitation method. Structural, magnetic, and photocatalytic properties of cobalt ferrites were analyzed according to their chemical composition considering their biological properties. XRD exhibited a spinel cubic structure without secondary phases. Using the SEM, the morphology of $CoFe_2O_4$ nanoparticles was examined and it was observed that the particles did not have a complete shape because they were agglomerated. The direct gap energies of the $CoFe_2O_4$ nanoparticles were observed as 2.1 eV. S-shaped magnetic hysteresis loop shows a soft ferromagnetic behavior. The coercivity field and magnetic saturation values of the $CoFe_2O_4$ nanoparticles at room temperate were 483 Oe and 60.39 emu/g, respectively. Photocatalytic properties of $CoFe_2O_4$ nanoparticles were investigated with three kinetic models. Among these, second-order kinetic model was found as the best relationship that fits the degradation of CV by $CoFe_2O_4$ nanoparticles. The theoretical concentration C_o (theory) obtained by second-order model (0.82 mg/L) fit with the experimental value of C_o (experimental) (0.95 mg/L). Based on this, it was concluded that $CoFe_2O_4$ nanoparticles would be suitable for use in wastewater treatment industries that clean organic dyes. Increasing intensity of absorption band at 408 nm and the precipitate showing a characteristic black color of heme–iron complexes were attributed to the strong oxidation of oxyhemoglobin to methemoglobin. $CoFe_2O_4$ nanoparticles showed undesirable hemolytic effect in both 1 mg/mL and 5 mg/mL concentrations. Undesirable hemolytic effect of $CoFe_2O_4$ nanoparticles on human erythrocytes at both concentrations was attributed to the comparatively high amount of reactive oxygen species formed by $CoFe_2O_4$ nanoparticles. The experimental results obtained proved that $CoFe_2O_4$ nanoparticles significantly increased the formation of methemoglobin, but also did not cause erythrocyte destruction (hemolysis). The biological incompatibilities of traditional iron oxide nanoparticles caused by the presence of iron in their structures have been reduced in $CoFe_2O_4$ nanoparticles where the cobalt is doped. It is known that spinel ferrite nanoparticles are of great importance in current techniques in both biomedical and industrial fields. It is hoped that this study will lead the way in the synthesis of nanoparticles with enhanced biocompatibility and sufficient magnetic and electrical properties with further research and modifications on $CoFe_2O_4$ nanoparticles.

Acknowledgements

This research was supported by the Research Fund of Bahcesehir University (BAU-BAP.2018.02.16 and BAP.2019.01.04), Istanbul.

References

1. G. Kandasamy, K. Kumar, *Synergy Between Nanoparticles and Breast Cancer Theranostics. Nanomedicines for Breast Cancer Theranostics* (Elsevier, Amsterdam, 2020), pp. 71–106
2. S. Nikazar, M. Barani, A. Rahdar, M. Zoghi, G.Z. Kyzas, Photo-and magnetothermally responsive nanomaterials for therapy, controlled drug delivery and imaging applications. ChemistrySelect **5**(40), 12590–12609 (2020)
3. Y. Wang, L. Zou, Z. Qiang, J. Jiang, Z. Zhu, J. Ren, Enhancing targeted cancer treatment by combining hyperthermia and radiotherapy using Mn–Zn ferrite magnetic nanoparticles. ACS Biomater. Sci. Eng. **6**(6), 3550–3562 (2020)
4. D. Maity, A. Sudame, G. Kandasamy, Superparamagnetic iron oxide nanoparticle-based drug delivery in cancer therapeutics, in *Nanobiotechnology in Diagnosis Drug Delivery and Treatment*. ed. by M. Rai, M. Razzaghi-Abyaneh, A.P. Ingle (Wiley, Hoboken, 2020), pp. 129–151
5. A. Sutradhar, Effects of Buoyant and Saffman lift force on magnetic drug targeting in microvessel in the presence of inertia. Microvasc. Res. **133**, 104099 (2020)
6. S.M. Dadfar, K. Roemhild, N.I. Drude, S. von Stillfried, R. Knüchel, F. Kiessling, T. Lammers, Iron oxide nanoparticles: diagnostic, therapeutic and theranostic applications. Adv. Drug Deliv. Rev. **138**, 302–325 (2019)
7. M.C. Chapman, A.Y. Lee, J.H. Hayward, B.N. Joe, E.R. Price, Superparamagnetic iron oxide sentinel node tracer injection: effects on breast MRI quality. J. Breast Imaging **2**(6), 577–582 (2020)
8. S. Kossatz, J. Grandke, P. Couleaud, A. Latorre, A. Aires, K. Crosbie-Staunton, M. Calero, Efficient treatment of breast cancer xenografts with multifunctionalized iron oxide nanoparticles combining magnetic hyperthermia and anti-

cancer drug delivery. Breast Cancer Res. **17**(1), 66 (2015). https://doi.org/10.1186/s13058-015-0576-1

9. U.T. Nakate, S.N. Kale, Microwave assisted synthesis and characterizations of $NiCo_2O_4$ nanoplates and electrical, magnetic properties. Mater. Today **3**(6), 1992–1998 (2016). https://doi.org/10.1016/j.jcis.2020.12.099
10. Q. Chang, H. Liang, B. Shi, X. Li, Y. Zhang, L. Zhang, H. Wu, Ethylenediamine-assisted hydrothermal synthesis of $NiCo_2O_4$ absorber with controlled morphology and excellent absorbing performance. J. Colloid Interface Sci. **588**, 336–345 (2021). https://doi.org/10.1016/j.jcis.2020.12.099
11. T.N. Pham, C.N. Van, D.N. Xuan, T.H. Van, P.N. Vu, L.N. Thi, A.T. Le, Roles of phase purity and crystallinity on chloramphenicol sensing performance of $CuCo_2O_4$/$CuFe_2O_4$-based electrochemical nanosensors. J. Electrochem. Soc. **168**, 026506 (2021)
12. A. Makridis, K. Topouridou, M. Tziomaki, D. Sakellari, K. Simeonidis, M. Angelakeris, O. Kalogirou, In vitro application of Mn-ferrite nanoparticles as novel magnetic hyperthermia agents. J. Mater. Chem. B **2**(47), 8390–8398 (2014). https://doi.org/10.1039/C4TB01017E
13. K. Islam, M. Haque, A. Kumar, A. Hoq, F. Hyder, S.M. Hoque, Manganese ferrite nanoparticles ($MnFe_2O_4$): size dependence for hyperthermia and negative/positive contrast enhancement in MRI. Nanomaterials **10**(11), 2297 (2020). https://doi.org/10.1149/1945-7111/abde80
14. N.P. Devi, M. Maisnam, Characterizations of sol–gel synthesized and high energy ball milled spinel nanoferrites: MFe_2O_4 (M= Li, Ni, Zn, Mn) for nanofluid preparations. Integr. Ferroelectr. **204**(1), 133–141 (2020)
15. M.K. Satheeshkumar, E.R. Kumar, P. Indhumathi, C. Srinivas, M. Deepty, S. Sathiyaraj, N. Suriyanarayanan, D.L. Sastry, Structural, morphological and magnetic properties of algae/CoFe2O4 and algae/Ag-Fe-O nanocomposites and their biomedical applications. Inorg. Chem. Commun. **111**, 107578 (2020)
16. M. Deepty, S. Ch, P.N. Ramesh, N.K. Mohan, M.S. Singh, C.L. Prajapat, A. Verma, D.L. Sastry, Evaluation of structural and dielectric properties of Mn^{2+}-substituted Zn-spinel ferrite nanoparticles for gas sensor applications. Sens. Actuators B **316**, 128127 (2020)
17. Y. Xu, Y. Ma, S. Xu, G. Zheng, Z. Dai, Diluted and undiluted monodispersed $CoFe_2O_4$ nanoparticles: the effects of post-annealing on magnetic properties. J. Mater. Sci. **50**(13), 4486–4494 (2015). https://doi.org/10.1007/s10853-015-8997-x
18. S. Yáñez-Vilar, M. Sánchez-Andújar, C. Gómez-Aguirre, J. Mira, M.A. Señarís-Rodríguez, S. Castro-García, A simple solvothermal synthesis of MFe_2O_4 (M = Mn, Co and Ni) nanoparticles. J. Solid State Chem. **182**(10), 2685–2690 (2009). https://doi.org/10.1016/j.jssc.2009.07.028
19. T.A. Tabish, M.N. Ashiq, M.A. Ullah, S. Iqbal, M. Latif, M. Ali, F. Iqbal, Biocompatibility of cobalt iron oxide magnetic nanoparticles in male rabbits. Korean J. Chem. Eng. **33**(7), 2222–2227 (2016). https://doi.org/10.1007/s11814-016-0043-4
20. D. Stanicki, L.V. Elst, R.N. Muller, S. Laurent, D. Felder-Flesch, D. Mertz, O. Ersen, Iron-oxide nanoparticle-based contrast agents, in *Contrast Agents for MRI*. ed. by V.C. Pierre, M.J. Allen (RSC, London, 2017), pp. 318–447
21. G.X. Wang, C.J. Liu, Y.M. Zhang, H.F. Peng, X. Wang, Characterization of nanosize Mn-Zn ferrites coated with citric acid. Adv. Mater. Res. **391**, 835–838 (2012)
22. K. Laznev, D. Tzerkovsky, K. Kekalo, G. Zhavnerko, V. Agabekov, IEEE. Trans. Magnet. **49**, 425 (2013)
23. K. Shahzad, S. Mushtaq, M. Rizwan, W. Khalid, M. Atif, F.U. Din, Z. Ali, Field-controlled magnetoelectric core-shell CoFe2O4@ BaTiO3 nanoparticles as effective drug carriers and drug release in vitro. Mater. Sci. Eng. C **119**, 111444 (2020)
24. B. Cai, M. Zhao, Y. Ma, Z. Ye, J. Huang, Bioinspired formation of 3D hierarchical CoFe2O4 porous microspheres for magnetic-controlled drug release. ACS Appl. Mater. Interfaces **7**(2), 1327–1333 (2015). https://doi.org/10.1021/am507689a
25. A. Manohar, C. Krishnamoorthi, C. Pavithra, N. Thota, Magnetic hyperthermia and photocatalytic properties of $MnFe_2O_4$ nanoparticles synthesized by solvothermal reflux method. J. Supercond. Nov. Magn. **34**(1), 251–259 (2021). https://doi.org/10.1007/s10948-020-05685-x
26. A. Manohar, C. Krishnamoorthi, K.C.B. Naidu, C. Pavithra, Dielectric, magnetic hyperthermia, and photocatalytic properties of ZnFe 2 O 4 nanoparticles synthesized by solvothermal reflux method. Appl. Phys. A **125**(7), 1–10 (2019). https://doi.org/10.1007/s00339-019-2760-0
27. N.A. Oladoja, E.T. Anthony, I.A. Ololade, T.D. Saliu, G.A. Bello, Self-propagation combustion method for the synthesis of solar active nano ferrite for Cr (VI) reduction in aqua system. J. Photochem. Photobiol. A **353**, 229–239 (2018)
28. L.A. Frolova, O.V. Khmelenko, The study of Co–Ni–Mn ferrites for the catalytic decomposition of 4-nitrophenol. Catal. Lett. (2020). https://doi.org/10.1007/s10562-020-03419-1
29. M. Rani, U. Shanker, A.K. Chaurasia, Catalytic potential of laccase immobilized on transition metal oxides nanomaterials: degradation of alizarin red S dye. J. Environ. Chem. Eng. **5**(3), 2730–2739 (2017). https://doi.org/10.1016/j.jece.2017.05.026

30. C. He, Z.Q. Shi, L. Ma, C. Cheng, C.X. Nie, M. Zhou, C.S. Zhao, Graphene oxide based heparin-mimicking and hemocompatible polymeric hydrogels for versatile biomedical applications. J. Mater. Chem. B **3**(4), 592–602 (2015). https://doi.org/10.1039/C4TB01806K
31. H.C. Fang, Z. Yang, C.K. Ong, Y. Li, C.S. Wang, Preparation and magnetic properties of (Zn–Sn) substituted barium hexaferrite nanoparticles for magnetic recording. J. Magn. Magn. Mater. **187**, 129–135 (1998). https://doi.org/10.1016/S0304-8853(98)00139-5
32. O.K. Mmelesi, N. Masunga, A. Kuvarega, T.T. Nkambule, B.B. Mamba, K.K. Kefeni, Cobalt ferrite nanoparticles and nanocomposites: photocatalytic, antimicrobial activity and toxicity in water treatment. Mater. Sci. Semicond. Process. (2021). https://doi.org/10.1016/j.mssp.2020.105523
33. M. Amiri, A. Akbari, M. Ahmadi, A. Pardakhti, M. Salavati-Niasari, Synthesis and in vitro evaluation of a novel magnetic drug delivery system; proecological method for the preparation of $CoFe_2O_4$ nanostructures. J. Mol. Liq. **249**, 1151–1160 (2018). https://doi.org/10.1016/j.molliq.2017.11.133
34. Y. Oh, M.S. Moorthy, P. Manivasagan, S. Bharathiraja, J. Oh, Magnetic hyperthermia and pH-responsive effective drug delivery to the sub-cellular level of human breast cancer cells by modified $CoFe_2O4$ nanoparticles. Biochimie **133**, 7–19 (2017). https://doi.org/10.1016/j.biochi.2016.11.012
35. X. Dong, B. Ren, Z. Sun, C. Li, X. Zhang, M. Kong, D.D. Dionysiou, Monodispersed $CuFe_2O_4$ nanoparticles anchored on natural kaolinite as highly efficient peroxymonosulfate catalyst for bisphenol A degradation. Appl. Catal. B **253**, 206–217 (2019). https://doi.org/10.1016/j.apcatb.2019.04.052
36. N. Verimli, A. Demiral, H. Yılmaz, M. Çulha, S.S. Erdem, Design of dense brush conformation bearing gold nanoparticles as theranostic agent for cancer. Appl. Biochem. Biotechnol. **189**(3), 709–728 (2019). https://doi.org/10.1007/s12010-019-03151-6
37. S.Y. Srinivasan, K.M. Paknikar, D. Bodas, V. Gajbhiye, Applications of cobalt ferrite nanoparticles in biomedical nanotechnology. Nanomedicine **13**(10), 1221–1238 (2018). https://doi.org/10.2217/nnm-2017-0379
38. M.C. Morán, A.F. Jorge, M.P. Vinardell, Sustainable DNA release from chitosan/protein based-DNA gel particles. Biomacromol **15**(11), 3953–3964 (2014). https://doi.org/10.1021/bm501039g
39. ISO 10993-4 (1992) Selection of tests for interaction with blood, International Standard Organization. Geneva, Switzerland
40. D. Zimmerman, J. Dienes, O. Abdulmalik, J.J. Elmer, Purification of diverse hemoglobins by metal salt precipitation. Protein Expr. Purif. **125**, 74–82 (2014). https://doi.org/10.1016/j.pep.2015.09.006
41. C.S. Silva, C. Moutinho, A. Ferreira da Vinha, C. Matos, Trace minerals in human health: iron, zinc, copper, manganese and fluorine. Int. J. Sci. Res. Methodol. **13**, 57–80 (2019)
42. A. Galanis, R. Karapetsas, Sandaltzopoulos Metal-induced carcinogenesis, oxidative stress and hypoxia signalling. Mutat. Res. **674**(1–2), 31–35 (2009). https://doi.org/10.1016/j.mrgentox.2008.10.008
43. A. Pichert, J. Arnhold, Interaction of the chlorite-based drug WF10 and chlorite with hemoglobin, methemoglobin and ferryl hemoglobin. Arch. Biochem. Biophys. **585**, 82–89 (2015). https://doi.org/10.1016/j.abb.2015.09.009
44. H.M. Shen, G.Y. Zhu, W.B. Yu, H.K. Wu, H.B. Ji, H.X. Shi, Y.B. She, Surface immobilization of β-cyclodextrin on hybrid silica and its fast adsorption performance of p-nitrophenol from the aqueous phase. RSC Adv. **5**(103), 84410–84422 (2015)
45. A.C. Gradinaru, G. Solcan, M.C. Spataru, L.D. Hritcu, L.C. Burtan, C. Spataru, The ecotoxicology of heavy metals from various anthropogenic sources and pathways for their bioremediation. Rev. Chim. **70**(7), 2556–2560 (2019)
46. S.C. Shen, A.B. Ley, Methemoglobin formation in human blood by cobalt in vitro. J. Clin. Investig. **33**(11), 1560–1566 (1954)
47. M. Adam, S. Murugavel, A. Bugyei-Twum, T. Narang, S. Jain, Y. Pan, K.K. Singh, BRCA2 is a novel regulator of endothelial cell function and apoptosis following oxidative stress. Atheroscler. Suppl. **32**, 110 (2018)
48. C. Fanelli, R. Zatz, Linking oxidative stress, the renin-angiotensin system, and hypertension. Hypertension **57**, 373–374 (2011). https://doi.org/10.1161/HYPERTENSIONAHA.110.167775
49. J. de Lara Andrade, A.G. Oliveira, V.V.G. Mariucci, A.C. Bento, M.V. Companhoni, C.V. Nakamura, D.M.F. de Oliveira, Effects of Al^{3+} concentration on the optical, structural, photocatalytic and cytotoxic properties of Al-doped ZnO. J. Alloys Compd. **729**, 978–987 (2017). https://doi.org/10.1016/j.jallcom.2017.09.128
50. S. Charles, S. Jomini, V. Fessard, E. Bigorgne-Vizade, C. Rousselle, C. Michel, Assessment of the in vitro genotoxicity of TiO_2 nanoparticles in a regulatory context. Nanotoxicology **12**(4), 357–374 (2018). https://doi.org/10.1080/17435390.2018.1451567
51. M.G. Nair, M. Nirmala, K. Rekha, A. Anukaliani, Structural, optical, photo catalytic and antibacterial activity of ZnO and Co doped ZnO nanoparticles. Mater. Lett. **65**(12), 1797–1800 (2011)
52. H. Tong, S. Ouyang, Y. Bi, N. Umezawa, M. Oshikiri, J. Ye, Nano photocatalytic materials: possibilities and challenges. Adv. Mater. **24**(2), 229–251 (2012)

53. G. Li, C. Guo, M. Yan, S. Liu, CsxWO_3 nanorods: realization of full-spectrum-responsive photocatalytic activities from UV, visible to near-infrared region. Appl. Catal. B **183**, 142–148 (2016)